# Learning hydrodynamic signatures through proprioceptive sensing by bioinspired swimmers

## Beau Pollard & Phanindra Tallapragada

200 EIB, Clemson University, Clemson, S.C., 29607, USA

E-mail: ptallap@clemson.edu

Abstract. Objects moving in water or stationary objects in streams create a vortex wake. Such vortex wakes encode information about the objects and the flow conditions. Underwater robots that often function with constrained sensing capabilities can benefit from extracting this information from vortex wakes. Many species of fish do exactly this, by sensing flow features using their lateral lines as part of their multimodal sensing. To replicate such capabilities in robots, significant research has been devoted to developing artificial lateral line sensors that can be placed on the surface of a robot to detect pressure and velocity gradients. We advance an alternative view of embodied sensing in this paper; the kinematics of a swimmer's body in response to the hydrodynamic forcing by the vortex wake can encode information about the vortex wake. Here we show that using artificial neural networks that take the angular velocity of the body as input, fish-like swimmers can be trained to label vortex wakes which are hydrodynamic signatures of other moving bodies and thus acquire a capability to 'blindly' identify them.

#### 1. Introduction

Mimicking the locomotion of fish and other aquatic swimmers has been a goal for underwater robotics research because of the many desirable characteristics of biological swimmers, such as energy efficiency, agility, and stealth [1–6]. A significant part of the agility and maneuverability of fish swimming can be attributed to the multimodal sensing of the fluid flow that provides information about surrounding objects in the flow in the absence of visual information [7–10]; in the most extreme cases blind fish can school quite well [7]. Flow information in this context could be one or more of the fluid velocity field, vorticity field, pressure distribution on a body or hydrodynamic force or moment experienced by a body. As an object moves in a fluid medium the surrounding fluid particles move relative to each other producing shear layers in the fluid which detach from the object resulting in the formation of a wake. Information about fluid flow and the objects that create these flows is encoded in the spatiotemporal evolution of the vortical structures, whether the body creating them are cylinders, airfoils, swimming, or flying creatures [11–19]. A problem of considerable interest in improving the sensory

suites of robots and their agility is whether a vortex wake created by a body can be sensed by a trailing robot to determine characteristics of the wake sources motion.

Fish extract such information about the source of a vortex field from the fluid flow using a grouping of mechanosensors, called the lateral line [20–27] which are made up of hundreds of neuromasts spread over their body that can detect subtle water motion and pressure gradients [28]. Considerable research and engineering has been devoted to creating artificial lateral lines through a variety of electromechanical sensors such as miniature pressure sensors [29–33], ionic polymer-metal composite sensors [34, 35], multi-layered silicon beams [36], and micro-fabricated hot-wire anemometry sensors [37]. While fish lateral lines and their artificial counterparts have received considerable attention, proprioceptive sensing, the ability to use the kinematics or motion of the body or parts of it to sense, has been unexplored in bioinspired swimming Proprioception has been demonstrated to be used by fish as part of their multimodal sensing. For instance, the rays and membranes of fins have been shown to act as mechanosensors in catfish [38], bluegill sunfish [39], and wrasses [40]. Fin mechanosensation has been found to encode the velocity of fin bending as well as respond to cyclic stimuli of biologically relevant frequencies with the mechanosensory system being capable of providing stroke by stroke feedback [41]. Such recent research in the proprioceptive ability of fish fins suggests that in the context of bioinspired robots, useful information about the flow and in particular the vortex field around a robot can be inferred from the kinematics of the robot or a part of it such as its tail. This would be significant because kinematic measurements such as acceleration and angular velocity can be made with high accuracy and temporal resolution using accelerometers, gyros or inertial measurement units (IMUs), which are inexpensive and robust compared to the pressure sensors used in artificial lateral lines [32]. Such kinematic measurements are usually made in most robots to provide feedback to control systems, but could potentially be used as a flow sensing measurement.

Extracting useful information about the fluid vortex field using even direct measurements of the fluid velocity field is, in general, a non-trivial problem [42–44]; extracting such information using only the kinematic information of a body immersed in the fluid is even more challenging due to the inherent complexities associated with coupled fluid-body dynamics. Machine learning can play an important role in deciphering the pertinent fluid flow information from the kinematic data of a moving body immersed in the fluid. Tools from machine learning have in the last decade been applied to decipher the complex dynamics of fluids, see for example [45] for a survey. In this paper we consider the important problem of a trailing fish-like body identifying and labeling vortex fields associated with different motions of another leading fish-like body. In a significant difference from many of the past papers on classification of flows through supervised learning which have usually used as input data the variables of fluid flow such as velocity, vorticity or pressure; we have chosen to use the kinematics of a body immersed in the fluid as the input data set for supervised learning. The trailing body can be taught to recognize different vorticity fields associated with different motions of

the leading body through supervised learning. In particular, artificial neural networks are well suited for this problem [46] because of the complex nonlinear phenomenon of vortex shedding and the interaction of a body with a vortex field.

To the authors' best knowledge, the only use of neural networks for classification of wakes created by Joukowski foils are found in [42–44]. The current paper draws upon the approach of using neural networks for wake classification in these papers [42–44]. In [42–44] the input information to the neural networks was obtained through immersed boundary layer or potential flow simulations and the input consisted of velocity, pressure, or vorticity measurements of the fluid in small regions around the body or directly in the flow field. Accurately recording these measurements from localized sensors can be difficult to obtain in practice especially outside a laboratory. On the other hand in this paper, the input data presented herein is obtained from experiments performed in a water tunnel which therefore makes no computational fluid dynamic modeling assumptions. The experimental input data is related to the kinematics of a trailing hydrofoil which is easily obtained using on-board sensors. The results in this paper can, therefore, be extended in the future to enable 'blind' steering of swimming robots.

## 2. Summary of Experiments

We created an experimental setup with two bioinspired hydrofoils placed in a water tunnel as shown in Fig. 1(a). The experiments were conducted in a Rolling Hills Research Corporation model 0710 water tunnel. The water tunnel has a working length of 45 cm and a testing cross-section of 450 cm<sup>2</sup> and is capable of producing laminar flow at speeds up to 7 cm/s. The trailing foil is modeled after a NACA 0030 airfoil with a chord length of 87.3 mm, and the leading foil has a chord length of 72.4 mm. The trailing foil is tethered to a bar of extruded aluminum, which doesn't contact the water; so the movement of the foil is solely the result of its body interacting with the vortex wake. The tether is a lightweight fishing line that is 10 mm long to limit the heaving motion in the trailing foil. The hydrofoil at the front of the water tunnel test section is oscillated by a Power HD servo controlled by an Arduino Mega. The leading hydrofoil is actuated to execute yaw oscillations in the free stream of the water tunnel with the angular orientation of the foil with respect to the free stream described by the equation

$$\theta_L = \theta_M \cos \frac{2\pi t}{f} \tag{1}$$

where  $\theta_M$  is the oscillation amplitude, t is time and f is the frequency of oscillations. The trailing hydrofoil is free to execute yaw oscillations in response to the hydrodynamic forcing created by the leading hydrofoil. The free stream velocity  $U_{\infty}$  in the water tunnel and the oscillations of the leading hydrofoil are controlled to produce unique vortex wakes which encode the information about the oscillations of the leading foil, see Fig. 1(b). The oscillations of the trailing foil are the response to the vortex wake created by the leading body, as shown in Fig. 1(c).

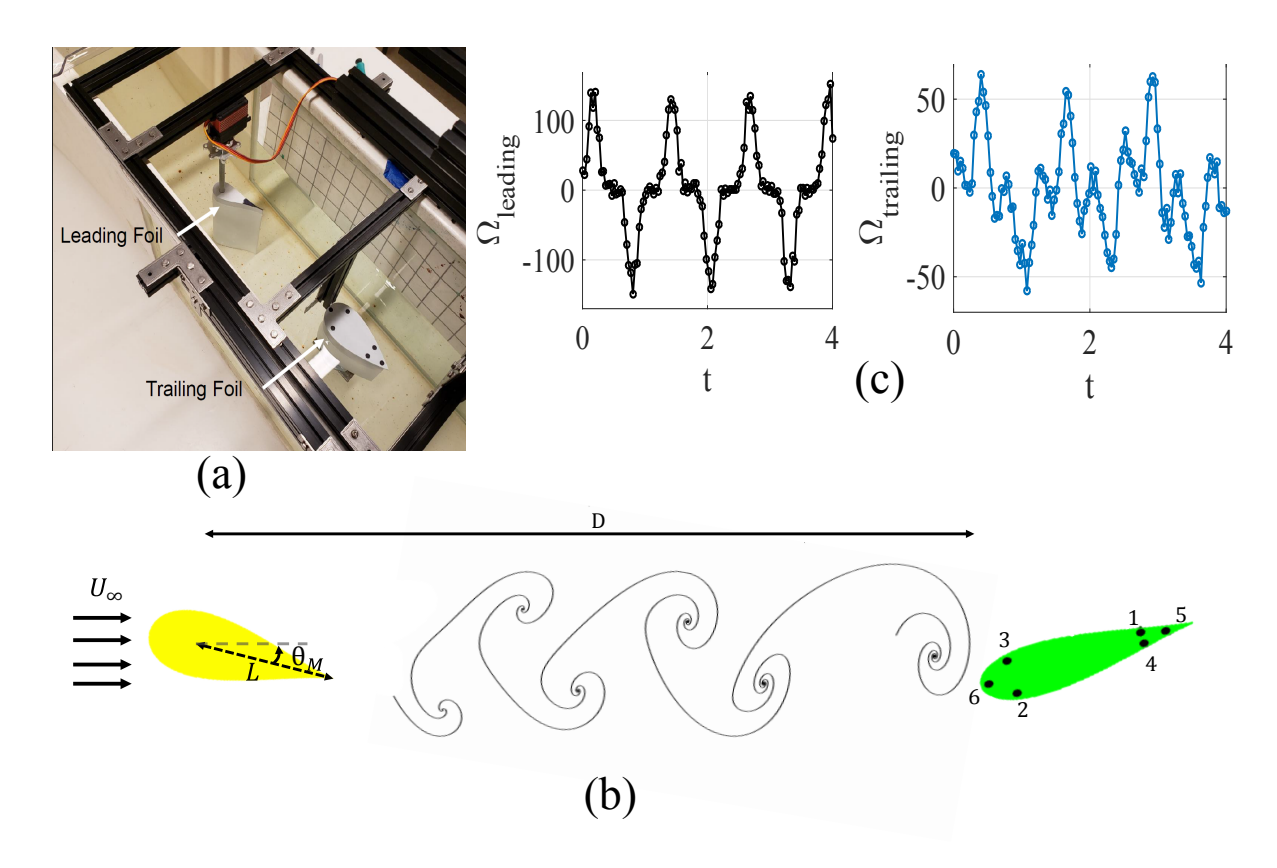


Figure 1: (a) Experimental setup showing the leading and trailing foils inside the water tunnel. (b) A schematic of the two foils with the vortex wake shed by the leading foil forcing the oscillatory response of the trailing foil. (c) Angular velocities of the of leading  $\Omega_L$  and  $\Omega_{trailing}$  from an experiment.

The vortex wakes are labeled by the Strouhal number, St defined as

$$St = \frac{f}{U_{\infty}} L \sin 2\theta_M \tag{2}$$

where L is the distance from the center of rotation to the trailing edge of the leading foil, as shown in Fig. 1(b). The non-dimensional Strouhal number, frequently used in fluid mechanics and specifically in the context of fish swimming to describe the periodic motion of the flapping bodies and the associated vortex wakes [47], is a suitable label that encodes information about the motion of the body generating the vortex wake for body Reynolds numbers ranging from  $10^3$  to  $10^8$  [18]. The Strouhal number, in this case, contains information about the frequency of the vortex shedding, the distance between the consecutively shed vortices, and the length of the source body that creates the vorticity. Sixteen different wakes, labelled 1 to 16 were created by altering f,  $\theta_M$  and  $U_{\infty}$  shown in the table 1 in increasing order of Strouhal number. The body Reynolds number using the length of the leading of foil and the free stream velocity range from 4437 to 6090. The Strouhal number range chosen in the experiments is intended to mimic the Strouhal numbers associated with efficient natural swimmers such as sharks,

Wake Class	Strouhal Number	f[Hz]	$U_{\infty} [\mathrm{m/s}]$	$\theta_M$ [°]
1	0.215	0.500	0.07	15
2	0.236	0.500	0.064	15
3	0.262	0.500	0.057	15
4	0.263	0.400	0.07	25
5	0.286	0.667	0.07	15
6	0.289	0.400	0.064	25
7	0.295	0.500	0.051	15
8	0.315	0.667	0.064	15
9	0.321	0.400	0.057	25
10	0.329	0.500	0.07	25
11	0.350	0.667	0.057	15
12	0.361	0.400	0.051	25
13	0.362	0.500	0.064	25
14	0.393	0.667	0.051	15
15	0.402	0.500	0.057	25
16	0.452	0.500	0.051	25

Table 1: The different combinations of input parameters and the associated Strouhal numbers. The free stream velocity was measured in inches/second in the water tunnel but it is converted here to the units m/s with an accuracy upto three decimal places.

dolphins, and bony fish which ranges from 0.2 to 0.45 [47].

## 2.1. Data Acquisition, Smoothing and Filtering

The trailing hydrofoil has six markers on its surface that are tracked in videos of the experiments. Videos of the trailing foil motion are recorded at a rate of 30 frames per second for a duration of 45 minutes each. Each experiment was recorded using the 12-megapixel rear facing camera on a Samsung Galaxy Note 9 fixed directly above the trailing foil. At each Strouhal number, 45 minutes of video data of the motion of the trailing foil was collected at a rate of 30 frames per second. The pixel locations of the six circle centers are calculated throughout the videos using a Hough transform implemented in MATLAB's image processing toolbox. Once the center locations are known we calculate the angle of lines connecting dots 1-2, 1-3, 4-2, 4-3, 5-2, 5-3, and 5-6 (shown in Fig. 1(b). The angular velocity is calculated using finite differencing between sequential camera frames and then the angular velocity from all seven measurements was averaged to get the average angular velocity of the foil between the camera snapshots.

The raw data of the angular velocity,  $x^{(j)}$  of the trailing foil is smoothed by a

three-point averaging method,

$$\overline{\mathbf{x}}_{i}^{(j)} = \frac{\mathbf{x}_{i-1}^{(j)} + \mathbf{x}_{i}^{(j)} + \mathbf{x}_{i+1}^{(j)}}{3} \tag{3}$$

Next, the data is passed through a low pass Butterworth filter with a cutoff frequency of 3Hz. The cutoff frequency was chosen such that it is at least four and a half times larger than any of the forcing frequency values. The output vector of column j from the Butterworth filter is  $\mathbf{x}^{(j)}$ , which is then normalized by,

$$\mathbf{x}_{\text{norm}}^{(j)} = \frac{(\mathbf{x}^{(j)} - \mu_{\mathbf{x}}^{(j)})}{\max(|(\mathbf{x}^{(j)} - \mu_{\mathbf{x}}^{(j)})|)}.$$
 (4)

In (4),  $\mu_{\mathbf{x}}^{(j)}$  is the mean of the entries in vector  $\mathbf{x}^{(j)}$ . The normalized angular velocity  $\mathbf{x}_{\text{norm}}^{(j)}$  is bounded to the interval [-1,1] independent of the distance D between the foils and the free stream velocity  $U_{\infty}$ . The normalization reduces this influence of the parameters D and  $U_{\infty}$  and ensures the combined effect through the Strouhal number St determines the response of the target foil.

Following the image processing of each frame in the video as explained in the Methods section the positions of the markers can be obtained allowing the calculation of the trailing foil's angular velocity. At each Strouhal number, the response of the trailing foil was measured at three different distances, D from the leading foil producing three 15 minute sets of data. These distances, measured from the shaft of the leading foil to the leading edge of the trailing foil, were 20.67cm, 23.2 cm, and 24.47 cm and are approximately three to four body lengths away from the leading foil. It can be expected that the hydrodynamic effect on the target foil is larger when this distance D is small and decreases as D increases.

Figure 1(c) shows a sample graph of the angular velocities of the leading foil and the trailing foil. The angular velocity of the leading foil is therefore not a pure sinusoid but instead has many harmonics because a stepper motor drives the motion of the leading foil and the fluid-body interactions resulting from the vortex wake [48]. Secondly the fluid-body interactions result in a non sinusoidal angular velocity on the foil even if a periodic torque is app Figures 2(a) and 2(b) show the power spectral density (plotted as decibels(dB)) of the angular velocities of the leading and trailing foil respectively for wake class 1 for D = 20.67cm. The local maxima in this plot correspond to the integer multiples of the forcing frequency f = 0.5 Hz. However, some of the harmonics in the response are missing, such as at 3 Hz and 4.5 Hz. As the free stream velocity,  $U_{\infty}$ , and the distance D change the relationship between the forcing and response frequency spectrum emerges to be more complicated. A plot of only the local maxima in the power spectral density for the set of wake classes  $\{1, 2, 3, 7\}$  is shown in Fig. 2(c). The distance D affects the magnitude (or amplitude) of the forcing by the vortex wake created by the leading foil, with the forcing decreasing as the distance increases. Frequency responses that scale linearly with the amplitude of forcing are a hallmark of linear systems. However, Fig. 2(c) shows that the response of the trailing foil at different

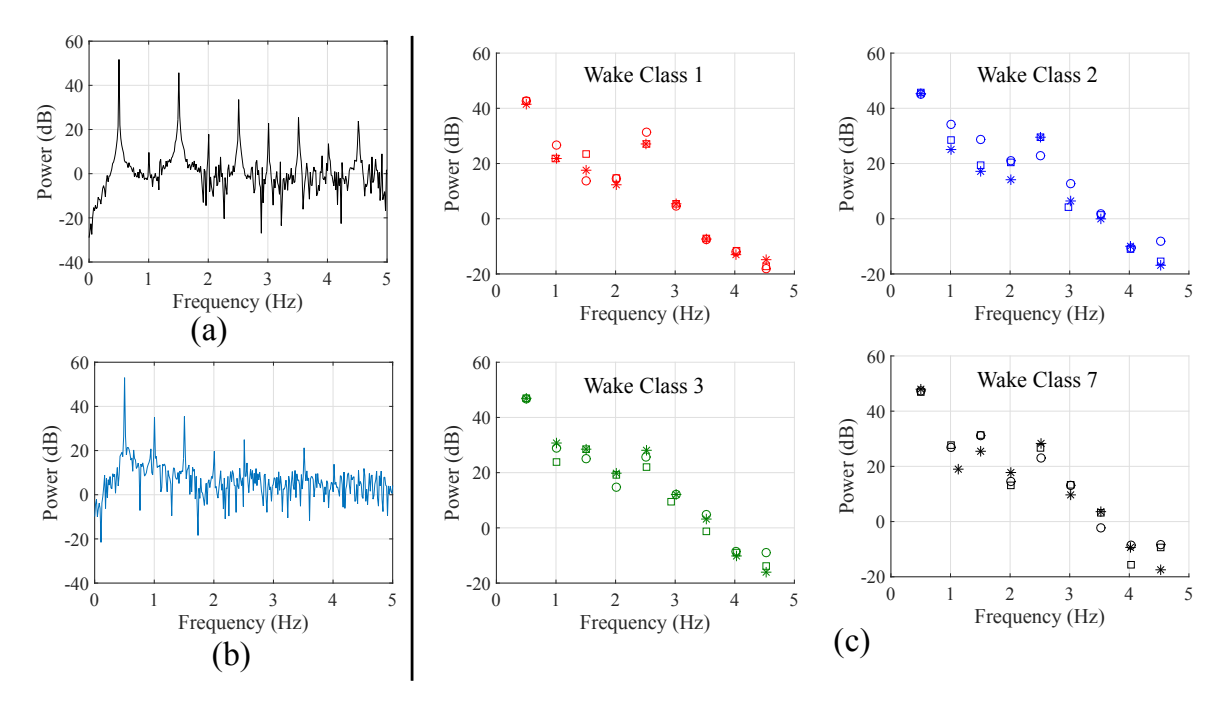


Figure 2: Power spectral density of the angular velocity of the (a) leading foil and (b) trailing foil for wake class 1 at D=20.67 cm. (c) The local maxima in the power spectral density of the angular velocity of the trailing foil for vortex wakes  $\{1, 2, 3, 7\}$  at three different distances  $D_1$ ,  $D_2$  and  $D_3$ . The vertical axis is power(dB). Legend - Response due to wakes of class 1 are in red, class 2 are in blue, class 3 are in green and class 7 are in black. Response at  $D_1$  are denoted by \*, at  $D_2$  by a  $\square$  and at  $D_3$  by  $\circ$ .

harmonics does not scale linearly with the distance. For example, the frequency response magnitude of the trailing foil is higher at distance  $D_2$  than at  $D_1$  at 1.5Hz for wake class 1; for wake class 2, the expected linear relationship is completely inverted at frequencies 1 and 1.5 Hz; for wake class 3 this inversion is seen at frequencies 1 Hz, 2 Hz and 2.5 Hz. The frequency response of the trailing foil for different wake classes in Fig. 2(c) shows a forcing amplitude dependence, that is characteristic of nonlinear systems. Proprioceptive wake classification therefore cannot be accomplished through standard frequency response analysis used in linear systems.

#### 3. Neural network architecture to classify the wakes

We used a neural network (NN) consisting of an input layer, one hidden layer, and an output layer as shown in Fig. 3. Each layer of the NN is fully connected to the previous layer. The input to the NN is a time series vector of filtered and smoothed angular velocity data of the trailing foil, represented throughout this paper by  $\tilde{\mathbf{x}}^k$  for kth data set. While each video data set for a wake label consists of  $N_f = 81000$  frames of images (15 minutes at 30 frames per second at 3 different distances D), each input vector consists of a small data set, that spans a time interval  $\Delta t$ . Four choices of the

variable  $\Delta t$  were made values of 1s, 2s, 3s or 4s with each choice of  $\Delta t$  being used to train a separate set of neural networks. With the free stream velocity  $U_{\infty}$  (see 1) used in these experiments, these values of  $\Delta t$  imply that vortex wake spanning one to four body lengths is used in the training, validation, and testing of NNs. The corresponding output from the neural network is a probability vector  $\tilde{\mathbf{y}}^k$  where each entry  $\tilde{y}^k_i$  is the probability that the wake label is i. The entirety of the inputs and outputs is represented by the matrices  $[\tilde{\mathbf{X}}]$  and  $[\mathbf{Y}]$  respectively,

$$\begin{bmatrix} \tilde{\mathbf{X}} \end{bmatrix} = \begin{bmatrix} | & | & \dots & | \\ \tilde{\mathbf{x}}^{(1)} & \tilde{\mathbf{x}}^{(2)} & \dots & \tilde{\mathbf{x}}^{(N)} \\ | & | & \dots & | \end{bmatrix}_{(30\Delta t \times N)} \quad \text{and} \quad \begin{bmatrix} \mathbf{Y} \end{bmatrix} = \begin{bmatrix} | & | & \dots & | \\ \mathbf{y}^{(1)} & \mathbf{y}^{(2)} & \dots & \mathbf{y}^{(N)} \\ | & | & \dots & | \end{bmatrix}_{(N_w \times N)}$$
(5)

where  $N_w = 16$  is the number of wake labels and  $N = \frac{N_f}{\Delta t}$ , the total number of input vectors, depends on  $\Delta t$ . To train the NN,  $[\tilde{\mathbf{X}}]$  is split into three unique subsets of data: training  $[\tilde{\mathbf{X}}_{\text{train}}]$ , validation  $[\tilde{\mathbf{X}}_{\text{valid}}]$  and testing  $[\tilde{\mathbf{X}}_{\text{test}}]$ . The sequence of the input column in vectors  $[\tilde{\mathbf{X}}_{\text{train}}]$  is randomized in each training epoch. The number of independent data vectors in the testing and validation data sets  $(N_{\text{test}}, N_{\text{valid}})$  each take 10% of the entire data set N, which leaves the remaining 80% for training  $(N_{\text{train}})$ . The first layer of the neural network contains  $N_1$  nodes and performs the affine linear

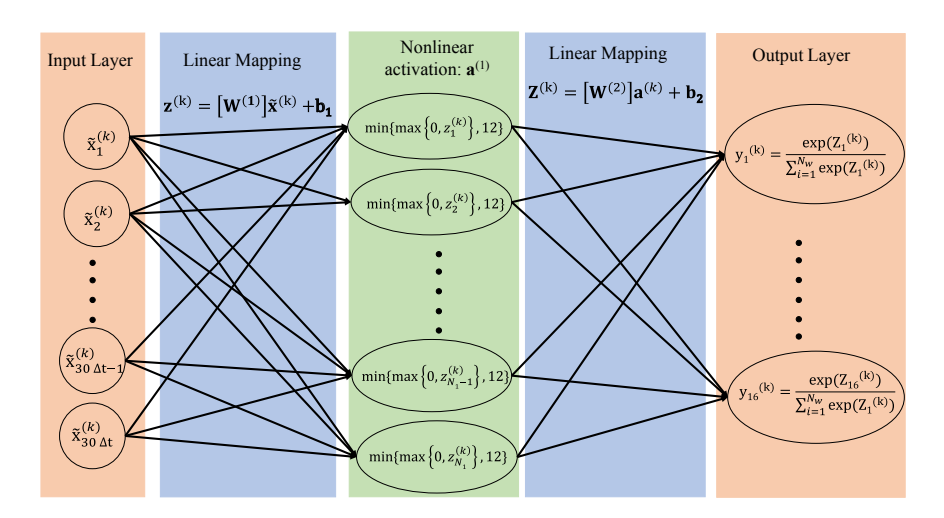


Figure 3: Architecture of the neural network used to classify vortex wakes. The inputs are the angular velocity of the trailing foil and the output is a probability vector for the wake labels. The sequence of the inputs are randomized in each epoch of training phases.

transformation  $\mathbf{z}^{(k)} = [\mathbf{W}_1]\tilde{\mathbf{x}}^{(k)} + \mathbf{b}_1$  with the  $N_1 \times 30\Delta t$  weight matrix  $[\mathbf{W}_1]$  and a  $30\Delta t \times 1$  bias vector  $\mathbf{b}_1$ . Each  $\mathbf{z}_1^{(k)}$  is passed through the Cutoff Rectified Linear Unit function (CReLU) activation function

$$\mathbf{a}^{(k)} = \min(\max(0, \mathbf{z}^{(k)}), 12). \tag{6}$$

The second layer of the network, begins with a linear transformation,

$$\mathbf{Z}^{(k)} = [\mathbf{W}_2]\mathbf{a}^{(k)} + \mathbf{b}_2 \tag{7}$$

where the weight matrix  $[\mathbf{W}_2]$  is of size  $[N_w \times N_1]$  and the bias vector  $\mathbf{b}^{(2)}$  is of size  $N_w \times 1$ . The output of this affine transformation eq.(7) is then input into the softmax activation function,

$$\tilde{\mathbf{y}}^{(k)} = \frac{\exp(\mathbf{Z}^{(k)})}{\sum_{i=1}^{N_w} \exp(\mathbf{Z}_i^{(k)})}.$$
(8)

The output  $\tilde{\mathbf{y}}^{(k)}$  is the probability vector whose *i*th entry  $\tilde{\mathbf{y}}_i^{(k)}$  is the probability that  $\tilde{\mathbf{x}}^{(k)}$  belongs to wake class *i*.

The performance of a neural network depends on the choice of the number of nodes in each layer and the initialization of the weighting and bias matrices/vectors,  $\Theta$ . The convergence of the weight matrices and bias vectors may also depend on the sequence of inputs used in the training. We changed the number of nodes in the first layer between 50 and 400. For each number of nodes  $N_1$ , we trained several (50 to 180) neural networks with varying initializations of the weight matrices and bias vectors. In each training iteration, the error in the classification is quantified using the cross-entropy error function, that allows fast training of neural networks [49]

$$C^{(k)} = -(\mathbf{y})^{\mathrm{T}} \ln(\tilde{\mathbf{y}}) - (1 - \mathbf{y})^{\mathrm{T}} \ln(1 - \tilde{\mathbf{y}}) + \frac{\eta}{N_p} \sum_{i=1}^{N_p} \Theta^2.$$
 (9)

The vector  $\Theta^2$  in (9) is the  $L_2$  regularization of all the NN parameters; it contains all of the entries in the weighting matrices and bias vectors. Once the error for iteration k is known, the weighting matrices and bias vectors are updated using the gradient descent method (10).

$$\begin{bmatrix} \mathbf{W}_1 \end{bmatrix}^{k+1} = \begin{bmatrix} \mathbf{W}_1 \end{bmatrix}^k - \epsilon \frac{\partial C^{(k)}}{\partial [\mathbf{W}_1]^k}, \quad \mathbf{b}_1^{k+1} = \mathbf{b}_1^k - \epsilon \frac{\partial C^{(k)}}{\partial \mathbf{b}_1^k}, \\
\begin{bmatrix} \mathbf{W}_2 \end{bmatrix}^{k+1} = \begin{bmatrix} \mathbf{W}_2 \end{bmatrix}^k - \epsilon \frac{\partial C^{(k)}}{\partial [\mathbf{W}_2]^k} \quad \text{and} \quad \mathbf{b}_2^{k+1} = \mathbf{b}_2^k - \epsilon \frac{\partial C^{(k)}}{\partial \mathbf{b}_2^k}
\end{bmatrix} \tag{10}$$

In (10),  $\epsilon$  is the learning rate of the neural network. For the first 40 iterations  $\epsilon = 0.002$ , after 40 iterations  $\epsilon$  is adjusted based on the change in C between iterations,

$$\epsilon = \begin{cases} \epsilon & \frac{\sigma_C}{\mu_C} < 5\\ \epsilon \times 0.75 & \frac{\sigma_C}{\mu_C} \ge 5 \end{cases} \tag{11}$$

where  $\sigma_C$  is the standard deviation in C between the last ten training iterations and  $\mu_C$  is the mean of C from the last ten training iterations. The purpose of adjusting the learning rate is to decrease the error in the final network while keeping the computational costs of training as low as possible.

In the validation phase the error for an individual data vector i is either zero or one. If the row with the largest entry of the output  $\tilde{\mathbf{y}}_{\text{valid}}^{i}$  corresponds to the row of  $\mathbf{Y}_{\text{valid}}^{i}$  containing a one then the error is  $C_{\text{valid}}^{i} = 0$  otherwise  $C_{\text{valid}}^{i} = 1$ . After every column of  $[\tilde{\mathbf{X}}_{\text{valid}}]$  has been pushed through the NN the total error is

$$C_{\text{epoch}}^{k} = \frac{1}{N_{\text{valid}}} \sum_{i=1}^{N_{\text{valid}}} C_{\text{valid}}^{i}$$
(12)

where the superscript k is the epoch number. To avoid overfitting the NN we used an early stopping method. Training is stopped when  $C_{\text{epoch}}^{k} < C_{\text{epoch}}^{k-1} < \dots < C_{\text{epoch}}^{k-20}$ , i.e. when total error,  $C_{\text{epoch}}$ , is increasing for 20 consecutive epochs. When the training is stopped the neural network corresponding to the k-20th epoch is chosen. The limit of 20 was set because in the initial iterations it is likely that the total error between epochs will fluctuate. The fluctuations could cause the NN to prematurely exit the training loop. Once the NN exits the training/validation loops we assess its accuracy when applied to the test data. We trained several hundred neural networks by back-propagating the cross-entropy error in each iteration. The results of the best neural network, the one with the highest accuracy, are presented in the next section.

#### 4. Results

The performance of each NN is quantified through a confusion matrix A. Figure 4 shows the confusion matrix A associated with the best performing NN. In Fig. 4, the entry  $\mathbf{A}_{i,j}$  represents the fraction of wake i sample that were classified as wake j. The diagonal elements of this matrix  $\mathbf{A}_{i,i}$  represent the fraction of correctly classified wakes of label i. For example  $A_{1,1} = 0.853$ , i.e. 85.3% of wake 1 samples were correctly classified by the NN as wake 1. The worst classification was for wake 13, where  $A_{13,13} = 0.706$ . In the case of four of vortex wake classes: 10, 13, 15, and 16 the accuracy of the NN is less than 0.8. The comparatively poor performance of the NN in classifying these wakes can be attributed to the large value of  $\theta_M = 25^{\circ}$  combined with the higher frequencies of oscillations associated with these wakes. The vortex wakes created in these cases collide with the water tunnel walls, rebound, and create more complex spatiotemporal patterns than in other cases. The differences in wake pattern between such cases and one with a more orderly pattern such as for wake type 7 is captured in the dye visualizations of the wakes in Fig. 5. We intentionally included vortex wakes with such complexity to incorporate significant effects of walls and other boundaries that will be encountered by a robot outside a lab environment.

We further performed statistical hypothesis testing on the classification shown in Fig. 7 to see how likely the classification was just a lucky outcome. We assumed the null hypothesis,  $H_0$  to be "the proposed Neural network model using the angular velocity of the target foil cannot classify the 16 different types of wakes". Under this null hypothesis, the probability that the *i*th angular velocity response of the target foil is of class j is 1/16 for all i and j, i.e every entry in the matrix  $\bf A$  should be  $\frac{1}{16}$ . We

	1	0.853	0.118	0.015	0.0	0.0	0.0	0.0	0.0	0.0	0.0	0.0	0.0	0.0	0.0	0.0	0.015
	2	0.147	0.824	0.029	0.0	0.0	0.0	0.0	0.0	0.0	0.0	0.0	0.0	0.0	0.0	0.0	0.0
	3	0.0	0.118	0.809	0.0	0.0	0.0	0.074	0.0	0.0	0.0	0.0	0.0	0.0	0.0	0.0	0.0
	4	0.0	0.0	0.0	0.926	0.0	0.074	0.0	0.0	0.0	0.0	0.0	0.0	0.0	0.0	0.0	0.0
on	5	0.0	0.0	0.0	0.0	0.897	0.0	0.0	0.103	0.0	0.0	0.0	0.0	0.0	0.0	0.0	0.0
at1	6	0.0	0.0	0.0	0.029	0.0	0.912	0.0	0.0	0.059	0.0	0.0	0.0	0.0	0.0	0.0	0.0
입	7	0.0	0.0	0.015	0.0	0.0	0.0	0.971	0.0	0.0	0.015	0.0	0.0	0.0	0.0	0.0	0.0
$^{\mathrm{SSI}}$	8	0.0	0.0	0.0	0.015	0.015	0.0	0.0	0.956	0.0	0.0	0.015	0.0	0.0	0.0	0.0	0.0
Classincation	9	0.0	0.0	0.0	0.015	0.0	0.162	0.0	0.0	0.809	0.0	0.0	0.015	0.0	0.0	0.0	0.0
- 1	10	0.015	0.0	0.0	0.0	0.0	0.0	0.0	0.0	0.0	0.750	0.0	0.0	0.132	0.0	0.103	0.0
Actual	11	0.0	0.0	0.0	0.0	0.0	0.0	0.0	0.029	0.0	0.0	0.882	0.0	0.0	0.088	0.0	0.0
ا <u>۲</u>	12	0.0	0.0	0.0	0.0	0.0	0.0	0.0	0.0	0.0	0.0	0.0	1.000	0.0	0.0	0.0	0.0
٦	13	0.0	0.0	0.0	0.0	0.0	0.0	0.0	0.0	0.0	0.103	0.0	0.0	0.706	0.0	0.162	0.029
	14	0.0	0.0	0.0	0.0	0.0	0.0	0.0	0.0	0.0	0.0	0.015	0.0	0.0	0.985	0.0	0.0
	15	0.0	0.0	0.0	0.0	0.0	0.0	0.0	0.0	0.0	0.103	0.0	0.0	0.059	0.0	0.735	0.103
	16	0.029	0.0	0.0	0.0	0.015	0.0	0.029	0.0	0.0	0.029	0.0	0.0	0.044	0.0	0.118	0.735
		1	2	3	4	5	6	7	8	9	10	11	12	13	14	15	16

Predicted Classification

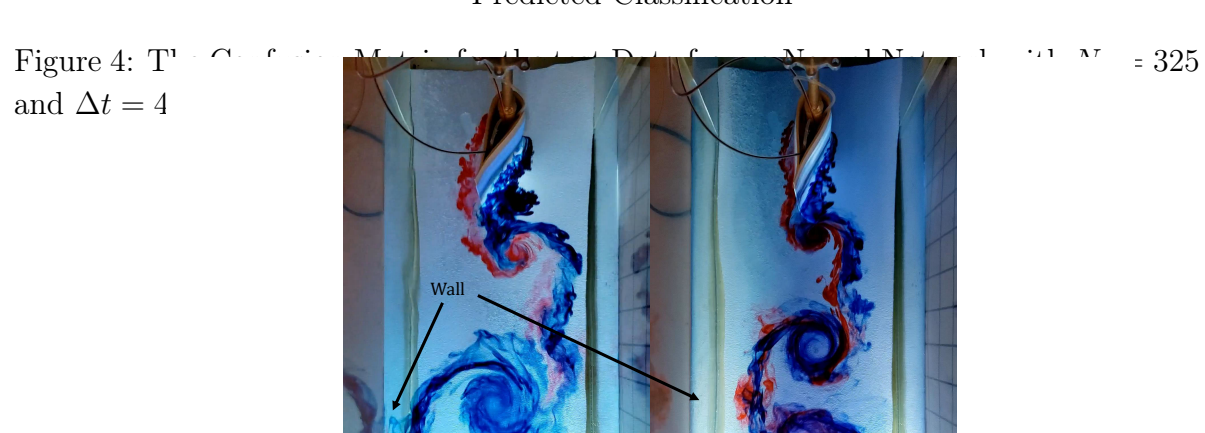


Figure 5: Dye visualizations of wake 16 (left) and 7 (right). The vortex wake in the left figure collides with the walls of the water tunnel while the one on the right has a width that is smaller than that of the water tunnel.

used the p-value to accept or reject the null hypothesis with the significance level,  $\alpha$  set at 5%, which is very commonly used. Using the  $\chi^2$  test, the p-value was found to be p=0.0104 which is below the chosen  $\alpha$  level. Therefore the null hypothesis is rejected. The value p=0.0104 implies that the probability that the null hypothesis being true is at most 0.0104. The observed confusion matrix in Fig. 7 would be extremely unlikely if the null hypothesis is true.

The variations in the accuracy of the 180 independent NNs trained on four-second data intervals is shown in Fig. 6. The blue boxes show the first and third quartile of the accuracy with the median shown by the red horizontal line. For instance, of the 180 NNs Fig. 6 shows that the highest accuracy of any of the NNs in classifying wake 13 is 0.81 and the lowest accuracy of the NNs is 0.37. The best NN (whose confusion matrix

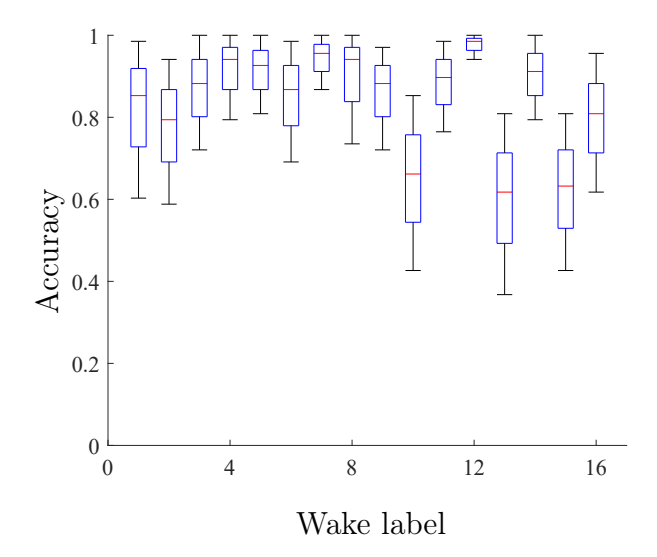


Figure 6: Whisker plot of the accuracy from the 180 independently trained NNs with a data truncation of  $\Delta t = 4$  on test data sets.

is shown in Fig. 4) was defined as one whose  $min(\mathbf{A}_{i,i})$  is the highest; i.e. where the lowest accuracy of classification of any wake was the highest amongst all the NNs. The whisker plot Fig. 6 shows that the largest variations in the accuracy of the NNs due to the variations in hyperparameters is for wakes 10, 13, 15 and 16 which are precisely the ones with the most complex spatiotemporal vortex wake patterns due to interference by walls of the water tunnel.

### Effect of frequency and amplitude of oscillations on the accuracy of NN

Errors arising in the classification of wake classes are influenced primarily by the frequency and amplitude of oscillations of the leading foil. For example, choosing cases wake classes 1, 2, 3, 7 have the same frequency (0.5Hz), and amplitude ( $\theta_M = 15^{\circ}$ ) of oscillations of the leading foil and differ only in the free stream velocity. An examination of rows 1, 2, 3 and 7 in the confusion matrix shows that mislabeling of these classes is confined to this same set of four wake classes. For example, wake class 3 when mislabeled is classified as either wake class 1, 2, or 7. Exceptions arise for mislabeling wake classes 1 and 7 with a small fraction of the wakes being classified as either wake class 10 or 16. Interestingly wake classes 10 and 16 have the same frequency, f = 0.5 Hz, but a different oscillation amplitude. A similar conclusion emerges when analyzing the classification of the two sets of wake classes  $\{4, 6, 9, 12\}$  and  $\{5, 8, 11, 14\}$  which have the same frequency and oscillation amplitude. Even in the set of wake classes  $\{10, 13, 15, 16\}$  where the vortex wake experiences significant wall effects, mislabeling of wakes is primarily confined to the same set of four wakes. For example, when wake 13 is wrongly labeled, it is mislabeled as wake 10, 15, or 16.

#### Effect of the choice of time interval

When the sample time interval  $\Delta t$  is smaller than one time period of oscillation of the leading foil, an insufficient amount of hydrodynamic information is transmitted to the trailing foil. Therefore it can be expected that for smaller values of  $\Delta t$ , the accuracy of the NN decreases. To assess the effect of the time interval,  $\Delta t$ , the accuracy the best performing NNs for each  $\Delta t$  as a function of the training epoch are shown in Fig. 7. The

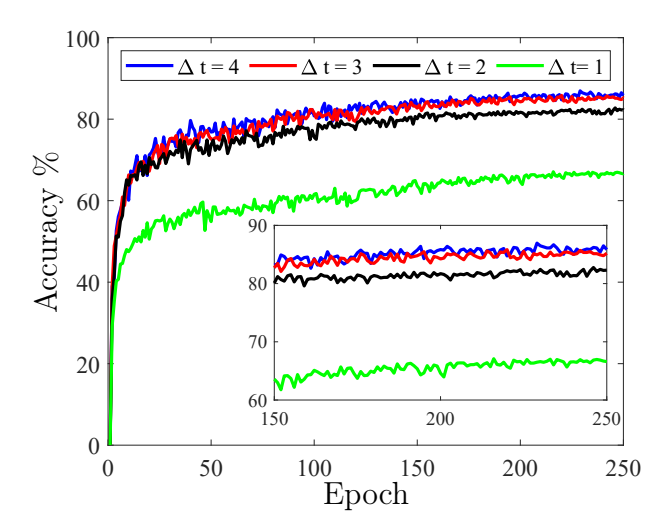


Figure 7: Accuracy of the best NN for each choice of  $\Delta t$  as a function of the training epoch.

accuracy of the NN for  $\Delta t = 1$  is about 17% lower than that of the NN with  $\Delta t = 2$ . This difference in accuracy emerges in less than 10 training epochs and persists even at 250 training epochs. The better accuracy as  $\Delta t$  increases is not an artifact of the number of training epochs. Moreover the gains in accuracy with increasing  $\Delta t$  decrease very rapidly with the accuracy for  $\Delta t = 4$  being only marginally higher than that for  $\Delta t = 3$ .

#### Discussion

We have presented a novel concept of using proprioceptive sensing data from a hydrofoil to classify vortex wakes created by the motion of a leading object. We verified this concept with experiments in a water tunnel with a periodically yawing leading foil and a trailing foil free to execute yaw oscillations due to the hydrodynamic forcing. The response of the trailing foil is nonlinear and, in general, the interaction between the foil and the fluid is complex thus rendering standard system identification tools of linear systems ineffective. An artificial neural network trained on experimental data of the angular velocity of the trailing foil can classify vortex wakes into 16 labels with accuracy ranging from 70.6% to 100%; with the lower accuracy values resulting for cases with a complex interaction of vortex wakes with the walls of the water tunnel.

The relevance of the results in this paper goes beyond the experiments described. The significance of the results are two fold. The first is that proprioceptive means using the kinematics of the passive segments of a swimming body can be used to sense and detect objects in the vicinity of the body. The second is that artificial neural networks could be used to train a swimming body to sense and identify objects by the vortex wakes they create. Moving objects in water display vortex signatures associated with their geometry and different gaits. Such 'blind' sensing and cognition can be incorporated into a multimodal sensing and cognition suite that can improve the low-level navigation and maneuvering ability of swimming robots. The findings in the paper are especially significant in the context of the underwater environment which imposes significant power limitations on many types of sensors or where requirements of stealth limit the use of other sensors. We also make the observation that in light of recent research showing that internal rotors not in contact with the water can propel a swimmer [50–53] and that passive tails can act as embodied controllers to improve the agility of swimming robots [54]; the findings in this paper suggest that passive tail or fin segments on a swimming robot could act as both embodied sensors and actuators.

The results in this paper motivate future paths to applications to underwater robots. The present paper focuses exclusively on the Strouhal number as a class label to establish that vortex wakes can be classified through proprioceptive means. One research direction that is suggested by this paper is the use of other other labels such as the body Reynolds number to further classify objects into sub classes that can identify leading body length or velocity scales. The second research direction is to adopt a transfer learning model, whereby model knowledge achieved in training on data sets of experiments in water tunnels could be used as a starting point to train on data sets. An intermediate step here could be the use of convolutional neural networks to first extract features in the kinematic data that relate to specific vortex wake features and apply this knowledge in transfer learning models. Lastly a path to applications is to directly train robots with a specific morphology to use their kinematic data to sense and identify vortex wakes.

## Acknowledgements

This work was partially supported by the NSF Grants CMMI 1563315 and 2021612.

#### References

- [1] M. S. Triantafyllou and G. Triantafyllou. An efficient swimming machine. *Scientific American*, 272(3):64, 1995.
- [2] M. S. Triantafyllou, G. S. Triantafyllou, and D. K. P. Yue. Hydrodynamics of fishlike swimming. *Annual Reviews of Fluid Mechanics*, 32:33–53, 2000.
- [3] J. E. Colgate and K. M. Lynch. Mechanics and control of swimming: a review. *IEEE Journal of Oceanic Engineering*, 29:660–673, 2004.
- [4] J. Liu and H. Hu. Biological inspiration: From carangiform fish to multi-joint robotic fish. *Journal of Bionic Engineering*, 7:35–48, 2010.

- [5] I. A. Ijspeert. Biorobotics: Using robots to emulate and investigate agile locomotion. *Science*, 346(6206):196–203, 2014.
- [6] E. Kelasidi, P. Liljeback, K. Y. Pettersen, and J. T. Gravdahl. Innovation in underwater robots: Biologically inspired swimming snake robots. *IEEE Robotics & Automation Magazine*, 23(1):44–62, 2016.
- [7] T. J. Pitcher, B.L. Partridge, and C. S. Wardle. A blind fish can school. *Science*, 194(4268):963–965, 1976.
- [8] B. L. Partridge and T. J. Pitcher. The sensory basis of fish schools: Relative roles of lateral line and vision. *Journal of Comparative Physiology*, 135(4):315–325, 1980.
- [9] J. C. Liao. A review of fish swimming mechanics and behaviour in altered flows. *Proceedings of the Royal Society B*, 362, 2007.
- [10] M. S. Triantafyllou, G. D. Weymouth, and J. Miao. Biomimetic survival hydrodynamics and flow sensing. *Annual Review of Fluid Mechanics*, 48(1), 2016.
- [11] C. H. K. Williamson and A. Roshko. Vortex formation in the wake of an oscillating cylinder. Journal of fluids and structures, 2(4):355–381, 1988.
- [12] T. Schnipper, A. Andersen, and T. Bohr. Vortex wakes of a flapping foil. *Journal of Fluid Mechanics*, 633:411–423, 2009.
- [13] K. Streitlien, G. S. Triantafyllou, and M. S. Triantafyllou. Efficient Foil Propulsion Through Vortex Control. *AIAA Journal*, 34:2315–2319, 1996.
- [14] F.E. Fish and G.V. Lauder. Passive and active flow control by swimming fishes and mammals. *Annu. Rev. Fluid Mech.*, 38:193–224, 2006.
- [15] E. D. Tytell and G. V. Lauder. The hydrodynamics of eel swimming: I. wake structure. *Journal of Experimental Biology*, 207(11):1825–1841, 2004.
- [16] I. K. Bartol, M. Gharib, P. W. Webb, D. Weihs, and M. S. Gordon. Body-induced vortical flows: a common mechanism for self-corrective trimming control in boxfishes. *Journal of Experimental Biology*, 208(2):327–344, 2005.
- [17] Frank Fish and GV Lauder. Not just going with the flow. American Scientist, 101(2):114–123, 2013.
- [18] M. Gazzola, M. Argentina, and L. Mahadevan. Gait and speed selection in slender inertial swimmers. Proceedings of the National Academy of Sciences of the United States of America, 112(13):3874–3879, 2015.
- [19] M. F. Platzer, K. D. Jones, J. Young, and J. C. S. Lai. Flapping wing aerodynamics: progress and challenges. *AIAA journal*, 46(9):2136–2149, 2008.
- [20] K. Pohlmann, F. W. Grasso, and T. Breithaupt. Tracking wakes: The nocturnal predatory strategy of piscivorous catfish. *Proceedings of the National Academy of Sciences*, 98(13):7371–7374, 2001.
- [21] K. Pohlmann, J. Atema, and T. Breithaupt. The importance of the lateral line in nocturnal predation of piscivorous catfish. *Journal of Experimental Biology*, 207(17):2971–2978, 2004.
- [22] T. J. Pitcher, B. L. Partridge, and C. S. Wardle. A blind fish can school. Science, 194(4268):963–965, 1976.
- [23] D.N. Beal, F.S. Hover, M.S. Triantafyllou, J.C. Liao, and G.V. Lauder. Passive propulsion in vortex wakes. *Journal of Fluid Mechanics*, 549:385–402, 2006.
- [24] J. Liao, D. Beal, G. Lauder, and M. Triantafyllou. The kármán gait: novel body kinematics of rainbow trout swimming in a vortex street. *Journal of experimental biology*, 206(6):1059–1073, 2003.
- [25] J. C. Liao. A review of fish swimming mechanics and behaviour in altered flows. *Philosophical Transactions of the Royal Society of London: B Biological Science*, 362(1487):19731993, 2007.
- [26] J. C. Liao. The role of the lateral line and vision on body kinematics and hydrodynamic preference of rainbow trout in turbulent flow. *Journal of Experimental Biology*, 209(20):4077–4090, 2006.
- [27] S. P. Windsor, S. E. Norris, S. M. Cameron, G. D. Mallinson, and J. C. Montgomery. The flow fields involved in hydrodynamic imaging by blind mexican cave fish (astyanax fasciatus). part i: open water and heading towards a wall. *Journal of Experimental Biology*, 213(22):3819–3831,

- 2010.
- [28] H. Bleckmann and R. Zelick. Lateral line system of fish. Integrative zoology, 4(1):13-25, 2009.
- [29] B. Free and D. A. Paley. Model-based observer and feedback control design for a rigid joukowski foil in a karman vortex street. *Bioinspiration & biomimetics*, 2017.
- [30] R. Venturelli, O. Akanyeti, F. Visentin, J. Ježov, L. D. Chambers, G. Toming, J. Brown, M. Kruusmaa, W. M. Megill, and P. Fiorini. Hydrodynamic pressure sensing with an artificial lateral line in steady and unsteady flows. *Bioinspiration & biomimetics*, 7(3):036004, 2012.
- [31] T. Salumäe and M. Kruusmaa. Flow-relative control of an underwater robot. *Proceedings of the Royal Society A: Mathematical, Physical and Engineering Sciences*, 469(2153):20120671, 2013.
- [32] F. D. Lagor, L. D. DeVries, K. Waychoff, and D. A. Paley. Bio-inspired flow sensing and control: Autonomous rheotaxis using distributed pressure measurements. *Journal of Unmanned System Technology*, 1(3):78–88, 2013.
- [33] D. F. Gomez, F. Lagor, P. B. Kirk, A. Lind, A. R. Jones, and D. A. Paley. Unsteady dmd-based flow field estimation from embedded pressure sensors in an actuated airfoil. In AIAA Scitech 2019 Forum, page 0346, 2019.
- [34] A.T. Abdulsadda and X. Tan. Nonlinear estimation-based dipole source localization for artificial lateral line systems. *Bioinspiration & biomimetics*, 8(2):026005, 2013.
- [35] A. T. Abdulsadda and X. Tan. An artificial lateral line system using ipmc sensor arrays. *International Journal of Smart and Nano Materials*, 3(3):226–242, 2012.
- [36] A. Qualtieri, F. Rizzi, G. Epifani, A. Ernits, M. Kruusmaa, and M. De Vittorio. Parylene-coated bioinspired artificial hair cell for liquid flow sensing. *Microelectronic Engineering*, 98:516–519, 2012.
- [37] Y. Yang, J. Chen, J. Engel, S. Pandya, N. Chen, C. Tucker, S. Coombs, D. L. Jones, and C. Liu. Distant touch hydrodynamic imaging with an artificial lateral line. *Proceedings of the National Academy of Sciences*, 103(50):18891–18895, 2006.
- [38] A. R. Hardy, B. M. Steinworth, and M. E. Hale. Touch sensation by pectoral fins of the catfish. Proceedings of the Royal Society B, 2016.
- [39] R. Williams, N. Neubarth, and M. E. Hale. The function of fin rays as proprioceptive sensors in fish. *Nature Communications*, 4:1729, 2013.
- [40] B. R. Aiello, M. W. Westneat, and M. E. Hale. Mechanosensation is evolutionarily tuned to locomotor mechanics. Proceedings of the National Academy of Sciences, 114:4459–4464, 2017.
- [41] B. R. Aiello, A. R. Hardy, M. W. Westneat, and M. E. Hale. Fins as mechanosensors for movement and touch-related behaviors. *Integrative and Comparative Biology*, 58(5):844–859, 2018.
- [42] B. Colvert, M. Alsalman, and E. Kanso. Classifying vortex wakes using neural networks. Bioinspiration & biomimetics, 13(2):025003, 2018.
- [43] M. Alsalman, B. Colvert, and E. Kanso. Training bioinspired sensors to classify flows. Bioinspiration & biomimetics, 14(1):016009, 2018.
- [44] M. Wang and M. S. Hemati. Detecting exotic wakes with hydrodynamic sensors. 33:235–254, 2019.
- [45] S. L. Brunton, B. R. Noack, and P. Koumoutsakos. Machine learning for fluid mechanics. Annual Review of Fluid Mechanics, 52:2020, 2019.
- [46] C. M. Bishop. Pattern recognition and machine learning. springer, 2006.
- [47] G. K. Taylor, R. L. Nudds, and A. L. R. Thomas. Flying and swimming animals cruise at a strouhal number tuned for high power efficiency. *Nature*, 425:707–711, 2003.
- [48] S. Y. Shinde and J. H. Arakeri. Physics of unsteady thrust and flow generation by a flexible surface flapping in the absence of a free stream.
- [49] P. Y. Simard, D. Steinkraus, and J. C. Platt. Best practices for convolutional neural networks applied to visual document analysis. In *International Conference on Document Analysis and Recognition*, volume 3, 2003.
- [50] P. Tallapragada. A swimming robot with an internal rotor as a nonholonomic system. *Proceedings* of the American Control Conference, 2015, 2015.

- [51] B. Pollard and P. Tallapragada. An aquatic robot propelled by an internal rotor. *IEEE/ASME Transaction on Mechatronics*, 22(2):931–939, 2017.
- [52] B. Pollard, V. Fedonyuk, and P. Tallapragada. Swimming on limit cycles with nonholonomic constraints. *Nonlinear Dynamics*, 97(4):2453 2468, 2019.
- [53] B. A. Free, J. Lee, and D. A. Paley. Bioinspired pursuit with a swimming robot using feedback control of an internal rotor. *Bioinspiration and Biomimetics*, 15(3):035005, 2020.
- [54] B. Pollard and P. Tallapragada. Passive appendages improve the maneuverability of fish-like robots. *IEEE/ASME Transactions on Mechatronics*, 24(4):1586–1596, 2019.